Lecture Notes for: Accelerator Physics and Technologies for Linear Colliders (University of Chicago, Physics 575) February 26^{th} and 28^{th}, 2002

Frank Zimmermann

CERN, SL Division

Contents

1 Beam-Delivery Overview

The beam delivery system is the part of a linear collider following the main linac. It typically consists of a collimation system, a final focus, and a beam-beam collision point located inside a particle-physics detector. Also the beam exit line required for the disposal of the spent beam is often subsumed under the term 'beam delivery'. See Fig. 1.

In addition, somewhere further upstream, there might be a beam switchyard from which the beams can be sent to several different interaction points, and possibly a bending section ('big bend') which provides a crossing angle and changes the direction of the beam line after collimation, so as to prevent the collimation debris from reaching the detector.

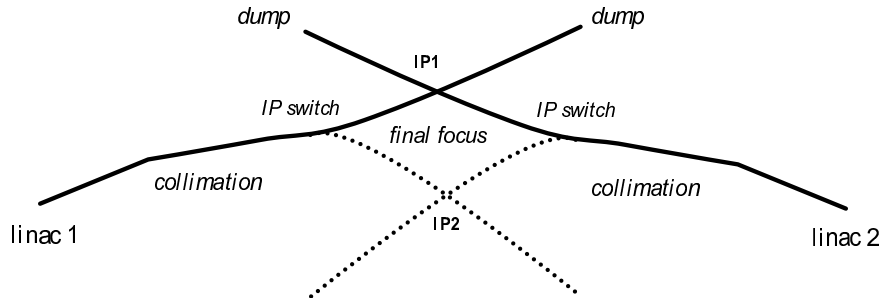

Figure 1: Schematic of the beam delivery system for a linear collider.

Table 1 lists typical beam and interaction-point parameters of various proposed linear collider projects. The numbers achieved at the SLC are included for comparison.

2 Collimation System

2.1 Halo Particles

If a beam particle passes the final quadrupoles in front of the collision point at a large transverse amplitude it can cause background in the physics detector, either by emitting synchrotron radiation or by being lost on a limiting aperture. The synchrotron radiation hitting the inner aperture of the quadrupoles or a mask, can be singly or doubly back-scattered into a sensitive part of the detector. Lost particles induce electro-magnetic showers. Both sources of background are undesirable. The common procedure of avoiding such background is to collimate the beams both in transverse (betatron) amplitudes and in energy upstream of the final-focus entrance in a dedicated collimation system.

Table 1: Beam and interaction-point parameters for various proposed linear colliders compared with those of the SLC. Note that some numbers may have changed since publication, and that, *e.g.*, TESLA now contemplates an alternative parameter set with higher luminosity. [†The SLC spot sizes quoted refer to the 1998 average values.]

Parameter	Symbol	SLC	TESLA	NLC	CLIC
C.m. energy [TeV]	E	0.1	0.5	1	3
Luminosity [10^{34} cm^{-2} s^{-1}]	L	0.0002	0.84	1.3	10
Repetition rate [Hz]	$f_{\rm rep}$	120	4	120	100
Bunch charge [10^{10}]	N_b	3.7	1.8	1.0	0.4
Bunches/rf pulse	n_b	1	2260	95	154
Bunch separation [ns]	Δ_b	—	354	2.8/1.4	0.67
Av. beam power [MW]	P_b	0.04	13	9	14.8
Bunch length [mm]	σ_z	1	0.5	0.12	0.03
Hor. emittance [μm]	$\gamma\epsilon_x$	50	12	4.5	0.68
Vert. emittance [μm]	$\gamma\epsilon_y$	8	0.03	0.1	0.02
Hor. beta [mm]	β_x^*	2.8	25	12	8
Vert. beta [mm]	β_y^*	1.5	0.5	0.15	0.15
Hor. spot size [nm]	σ_x^*	1700†	783	235	43
Vert. spot size [nm]	σ_y^*	900†	5.5	4	1.0
Upsilon	Υ	2×10^{-3}	0.02	0.3	8.1
Pinch enhancement	H_D	2.0	1.6	1.45	2.24
Beamstrahlung	δ_B [%]	0.06	1.0	10	31
Photons per $\rm e^-$ ($\rm e^+$)	N_γ	1	0.9	1.4	2.3

2.2 Functions of Collimation System

In addition to removing the large-amplitude or off-energy 'halo' particles, the collimation system should fulfill several other functions, namely:

- The collimators should protect the downstream beamline components against mis-steered beams in case of a subsystem failure, and ideally survive the impact of a full bunch train.
- The collimator wake fields should not significantly amplify a trajectory change or blow up the beam size.
- The collimation should be sufficiently far away from the collision point to allow for a suppression of the number of muons generated by the collimation.

2.3 Collimator Survival

One of the greatest challenges in the design of the collimaton system is the requirement that the system should survive the impact of a full bunch train. (For TESLA it only needs to survive a few bunches, as the pulse length is so long that later bunches can be either stopped in the damping ring or sent through a bypass line directly onto the dump.) Collimator survival was already a difficult challenge at the SLC; see Fig. 3.

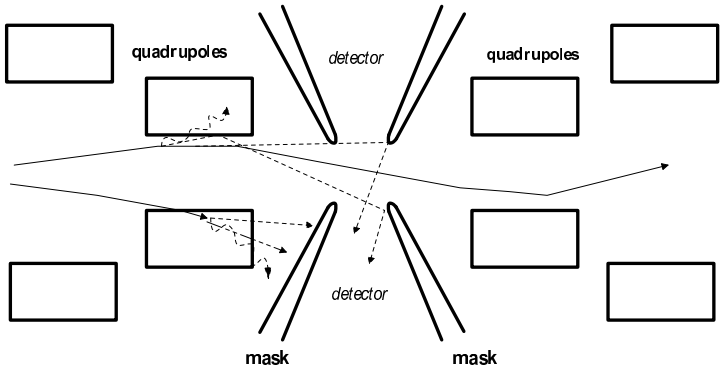

Figure 2: Beam loss in the final quadrupoles or synchrotron radiation emitted by halo particles may cause unwanted background in the detector.

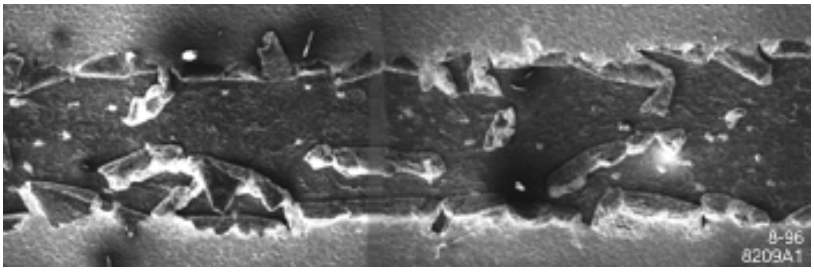

Figure 3: Picture of a damaged SLC collimator. The 20-μm thick gold coating on top of a Ti alloy was completely ablated by beam impact. The grooves formed by the beam extended well into the Ti substrate. The rough surface of the damaged collimators gave rise to severe wake-field effects. (Courtesy F.-J. Decker)

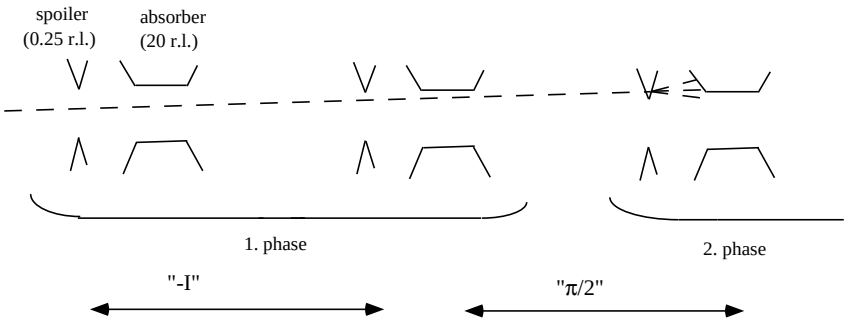

Figure 4: Schematic of a conventional collimation system consisting of a series of spoilers followed by absorbers. The size of the spoilers and absorbers is 0.25–1 and 20 radiation lengths, respectively. Collimation is performed in both betatron phases as indicated.

The conventional approach of dealing with this problem is to build a dual system consisting of short spoilers (*i.e.*, of 0.25–1 radiation lengths) followed downstream by long (10–20 radiation lengths) absorbers. This is illustrated in Fig. 4.

In the spoiler, the beam particles undergo multiple scattering. The horizontal and vertical rms scattering angles are

$$\theta_0 \approx \left(\frac{14\ \mathrm{MeV}/c}{p}\right)\sqrt{\frac{s}{X_0}}\ , \tag{1}$$

where c is the speed of light, p the particle momentum, s the thickness of the spoiler, and X_0 its radiation length. Since the spoiler is at a location with large beta functions, and since the beam emittance is small, the rms angle θ_0 is much larger than the initial beam divergence $\sqrt{\epsilon/\beta}$.

Suppose an absorber is placed a distance L downstream of the spoiler. A beam hitting this absorber (which first must have passed through the spoiler) will have a size of about

$$(\sigma_x \sigma_y)_{\mathrm{absorber}} \approx L^2\theta_0^2\ . \tag{2}$$

Choosing the distance L large enough, it is possible to obtain a beam size of a few square millimeters, adequate to guarantee absorber survival.

It turns out that the survival of the spoilers is more difficult to guarantee. Although the spoilers are sufficiently thin that no full electro-magnetic shower can develop, the spoilers can still be damaged by surface fracture, if the local temperature increases beyond an acceptable limit.

The temperature increase is

$$\Delta T = \frac{1}{C_p}\frac{\Delta\mathcal{E}}{\Delta m}\ , \tag{3}$$

where C_p is the heat capacity, and $\Delta\mathcal{E}$ the energy deposited by the beam into a mass Δm.

The temperature change will lead to a change in the length of the material via

$$\frac{\Delta s}{s} = \alpha \Delta T \tag{4}$$

where α is the thermal expansion coefficient. The change in length in turn is related to a tension via Hooke's law:

$$\sigma = E\left(\frac{\Delta s}{s}\right) = E\alpha\Delta T = E\alpha\frac{1}{C_p}\frac{\Delta\mathcal{E}}{\Delta m}\,. \tag{5}$$

Here E is the elastic or Young's module. The surface withstands a beam impact if

$$\sigma < \sigma_{\rm UTS}\ , \tag{6}$$

where $\sigma_{\rm UTS}$ denotes the ultimate tensile strength of the material in question.

In order to express the energy deposition in terms of the beam particles and beam size. we only consider the energy transfer by ionization, characterized by the parameter '$(d\mathcal{E}/dx)$', and find

$$\frac{\Delta\mathcal{E}}{\Delta m} = \frac{(d\mathcal{E}/dx)N_b n_b}{\rho 2\pi\sigma_x\sigma_y}\,. \tag{7}$$

Combining Eqs. (5), (6), and (7), we finally obtain

$$(\sigma_x\sigma_y) > \frac{1}{2\pi}\left(\frac{d\mathcal{E}}{\rho\,dx}\right)N_b n_b\frac{E\alpha}{C_p}\frac{1}{\sigma_{\rm UTS}}\,. \tag{8}$$

As an example, assuming the material properties of copper, $\alpha = 1.7\times10^{-5}$ K^{-1}, $E = 120$ GPa, $C_p = 0.385$ Jg^{-1}K^{-1}, $d\mathcal{E}/(\rho\,dx) \approx 1.44$ MeV cm^2/g, and $\sigma_{UTS} = 300$ MPa, we find

$$(\sigma_x\sigma_y)^{1/2} \geq 200\ \mu{\rm m} \quad \text{or} \quad \beta_{x,y} \geq 1500\,{\rm km},$$

where, in the last step, we considered normalized emittances of $\gamma\epsilon_x = 0.68$ μm and $\gamma\epsilon_y = 0.01$ μm at 1.5-TeV beam energy. Beta-functions of 1000s of km imply a long system and tight tolerances.

Our above estimate is still somewhat optimistic, since we have ignored the onset of the shower inside the spoiler, which will enlarge the actual energy deposition, as well as the heating of the collimator surface by beam image currents.

2.4 Muons

If halo particles are scraped off at the collimators, a new source of background is generated: muons. About one muon is created per 10^4 lost electrons (mainly by the so-called Bethe-Heitler process). The muons are highly energetic and only weakly interact with matter. If no further measures are taken, many muons will propagate inside the tunnel almost parallel to the beam and pass through the detector. The harsh muon background was one of the unexpected surprises during the early days of SLC operation. In an attempt to render this muon background acceptable, several sets of new collimators as

well as muon toroids were installed at the end of the linac, in the SLC arcs, and in the final focus.

Usually, a large distance between collimation and detector reduces the number of muons reaching the latter. The muons can also be slowed down and deflected by installing 10s of meters of 'tunnel fillers', weighing 1000s of tons and comprising magnetized toroids, in which the muons simultaneously lose energy and are bent. These tunnel fillers potentially reduce the muon background by one or two orders of magnitude.

The largest uncertainty in our estimates of muon background for a future collider is the incomplete knowledge of the beam halo. While rough analytical estimates suggest that the unavoidable halo, *e.g.*, due to gas scattering, could be negligibly small, at the SLC often up to several percent of the beam had to be collimated. The source of the SLC halo was not understood. If at a future collider, 0.1% of the beam must be collimated, the number of primary muons will be huge.

Figure 5 shows the simulation of a supersymmetric event in CLIC together with muon background traversing the detector (1650 tracks). If a halo of 10^{-3} (beam fraction) is collimated, the number of muon tracks per bunch train would be 15 times higher than shown.

2.5 Downstream Sources of Beam Halo

There are two primary sources of beam halo which cannot be avoided, and which may re-generate halo after the beam has already been collimated: (1) beam-gas bremsstrahlung, and (2) Compton scattering on black-body radiation.

The cross section for bremsstrahlung, *i.e.*, inelastic scattering off the residual gas, with a relative energy loss larger than δ_m is

$$\sigma_{\rm brems} \approx -\frac{16}{3} r_e^2 \alpha Z^2 \ln \delta_m \ln\left(\frac{183}{Z^{1/3}}\right) \tag{9}$$

where Z is the atomic number of the gas component, α the fine structure constant, and r_e the classical electron radius. Note that this cross section is independent of the beam energy, and thus, unlike elastic scattering, remains important at the highest energies. For $\delta_m = 1\%$, and N_2 (or CO), one has $\sigma_{\rm brems} \approx 6$ barn. Assuming 1 ntorr CO pressure at room temperature, the molecular density is $\rho_{CO} \approx 3 \times 10^{13}$ m^{-3}.

The total cross section for scattering on thermal photons is close to the Thomson cross section $\sigma_{\rm th} \approx 8\pi r_e^2/3 \approx 0.7$ barn. At room temperature, the density of photons is about $\rho_\gamma \approx 5 \times 10^{14}$ m^{-3}.

The fraction of beam particles scattered over a distance L is

$$\frac{\Delta N}{N} = \sigma \rho L \tag{10}$$

where σ is the cross section (*e.g.*, equal to $\sigma_{\rm brems}$ or $\sigma_{\rm th}$) and ρ the density (equal to ρ_{CO} or ρ_γ).

One finds that 1 ntorr CO pressure is roughly equivalent to the effect of the thermal photons at room temperature. Typically several hundred scattering events may occur

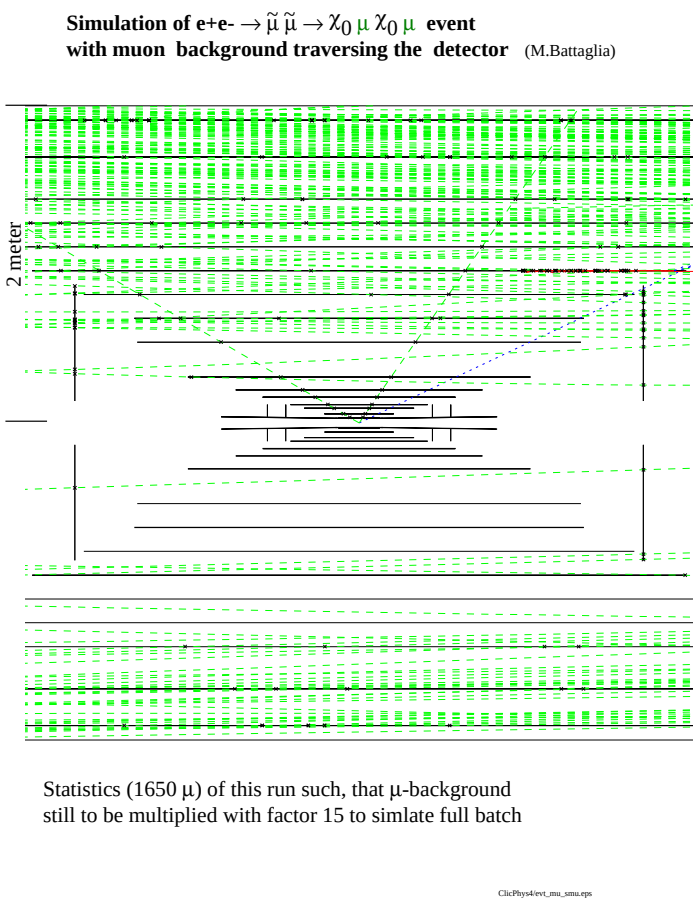

Figure 5: Simulation of an event $e^+e^- \rightarrow \tilde{\mu}\tilde{\mu} \rightarrow \chi_0\mu\chi_0\mu$ together with 1650 background muon tracks traversing the detector. (Courtesy M. Battaglia and H. Burkhardt)

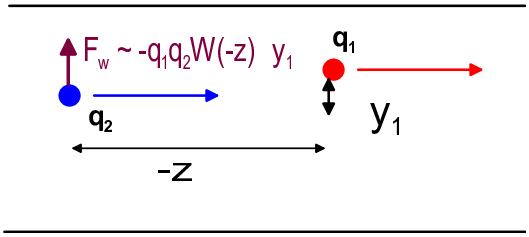

Figure 6: Illustration of a transverse wake field excited by a leading particle, which deflects the tail particle.

per bunch train in a few-km long beam delivery system. A large part of the scattered particles can be intercepted by secondary collimators in the final focus.

2.6 Collimator Wake Fields

Since the beam sizes are small, the collimator gaps tend to be small as well. As a consequence a beam which is not perfectly centered in such a collimator can excite a strong wake field by which it is further deflected from the axis. Such wake-field induced jitter amplification was a serious problem at the SLC.

Figure 6 illustrates the concept of a transverse wake field and it introduces the wake function $W(z)$ which describes the strength of the transverse wake force at a distance z behind the source. Leading particles which are offset generate an electric or magnetic field which deflects the following particles. In a geometry with cylindrical symmetry, the strength of the deflection depends only on the longitudinal distance between the two particles and it varies linearly with the offset of the leading particle, whereas it is independent of the position of the deflected particle.

Assuming that the beam offset Δy is constant along the bunch, the deflection of a beam slice at position z is obtained by integrating the wake field generated by all the leading slices (with $z' > z$):

$$\Delta y'(z) = -\frac{r_e N_b \Delta y}{\gamma} \int_z^\infty W(z - z')\rho(z')dz' \tag{11}$$

where $\rho(z)$ denotes the normalized charge distribution along the bunch ($\int dz\ \rho(z) = 1$).

The centroid deflection of the beam is obtained by averaging the wake-field deflection over the longitudinal beam distribution:

$$< \Delta y' >= \int_{-\infty}^{\infty} \rho(z)\Delta y'(z)dz\ . \tag{12}$$

In addition to the centroid deflection, the wake field will also increase the beam divergence and hence the projected beam emittance, which can be calculated by averaging the square of $\Delta y'(z)$ (and subtracting from this the squared average). In the following

we will always refer to the centroid deflection of one entire bunch, dropping the angular brackets.

At a collimator gap, there exist two types of wake fields: (1) those arising from the finite resistivity of the chamber, and (2) those arising from the change in geometry, *i.e.*, from a variation in aperture. To minimize the second, geometric wake field, a typical collimator is tapered as illustrated in Fig. 7.

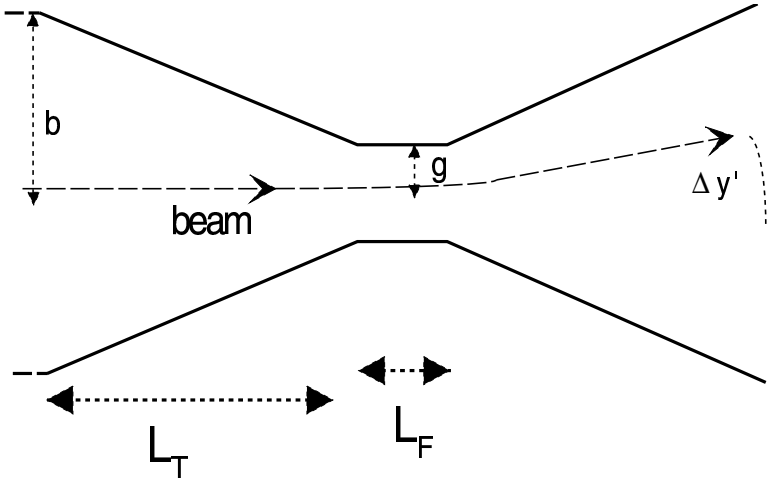

Figure 7: Schematic of a tapered collimator. If the beam passes off-center, it will be deflected by the collimator wake field.

The central flat part of the collimator only gives rise to a resistive wake. The deflection of the bunch centroid in a round collimator with radius g and a flat length L_F is

$$\Delta y'_F = 0.816\, L_F \frac{N_b r_e}{\gamma \sigma_z} \frac{2}{g^3} \sqrt{\lambda \sigma_z}\, \Delta y \tag{13}$$

where Δy is the offset from the pipe center, and $\lambda[\mathrm{m}] \equiv \rho[\Omega\mathrm{m}]/(120\pi)$ is referred to as the resistive depth (ρ is the resistivity in units of Ωm).

We note that the longitudinal resitive-wall impedance (the Fourier transform in time of the point-source wake field) can be estimated as

$$Z_{||} = \frac{C}{2\pi g} \mathcal{R}_{\mathrm{surf}} \tag{14}$$

where $\mathcal{R}_{\mathrm{surf}}$ is the surface impedance in units Ω per square meter (and this in turn is equal to $(1+i)\rho/\delta_s$ with ρ the resistivity and δ_s the skin depth). Since the transverse impedance is related to the longitudinal via

$$Z_{\perp} = \frac{2c}{g^2} \frac{Z_{||}}{\omega}\,, \tag{15}$$

this results in the $1/g^3$ dependence of the transverse wake field, which we have quoted in Eq. (13).

Consider now a collimator which is tapered on either side under a shallow angle θ ($\theta \ll 1$). The taper may extend over a length L_T (on either side) after which the beam pipe reaches the nominal aperture b. We assume that $b \gg g$. The wake field of the taper (adding both outgoing and incoming side) is the sum of a geometric and a resistive part:

$$\Delta y'_T = \frac{2N_b r_e}{\gamma \sigma_z} \left(\frac{1}{2\sqrt{\pi}} \frac{2b}{gL_T} + 0.816 L_T \frac{1}{bg^2} \sqrt{\lambda \sigma_z} \right) \Delta y \tag{16}$$

The resistive part can be obtained by integrating the formula (13) over a length with varying radius, the geometric wake was derived by K. Yokoya.

Finally, the total deflection by the collimator wake field is the sum of the contributions from the flat part and from the taper:

$$\Delta y' = \Delta y'_T + \Delta y'_F \, . \tag{17}$$

The deflection can be minimized by (1) optimizing the length of the taper, (2) selecting the material, (3) choosing an optimum value for the gap g.

Note that all the expressions above refer to round collimators, for which exact expressions of the wake fields are available (except perhaps for a rigorous proof that one can linearly add the geometric and the resistive wake fields for the tapered part). On the other hand, for flat rectangular collimators the theory has been more uncertain. A few years ago the calculated wake fields for flat tapered collimators varied between zero and infinity. In the meantime, a wake-field test facility has come under operation at SLAC, and new experimental data appear to be converging against updated theoretical predictions.

2.7 Collimation Optics

The collimation systems for most collider designs are based on a simple linear optics consisting of FODO cells. For the energy collimation also bending magnets are needed in order to generate dispersion. These dispersive regions can simultaneously be used for chromatic correction by means of sextupole magnets. Pairs of sextupoles separated by a phase advance of 180° ('$-I$ transformation') are particularly popular, since they lead to an automatic cancellation of geometric aberrations. This is illustrated in Fig. 8. We will discuss the $-I$ transformation in Section 3.3.

For a linear collimation system, the collimator gap is given by the rms beam size σ at the spoiler and the desired collimation depth n (in units of σ), *e.g.*, in the vertical plane:

$$g_y = n_y \sigma_{\mathrm{spoiler},y} = n_y \sqrt{\beta_{y,\mathrm{spoiler}} \epsilon_y} \, . \tag{18}$$

In addition to the purely linear collimation systems just described, various types of nonlinear systems have been explored. The nonlinear schemes offer a number of potential advantages, as they could (a) blow up the beam size at the spoiler, (b) increase the collimator gap and reduce the wake-field effects, (c) fold in the beam tails at the

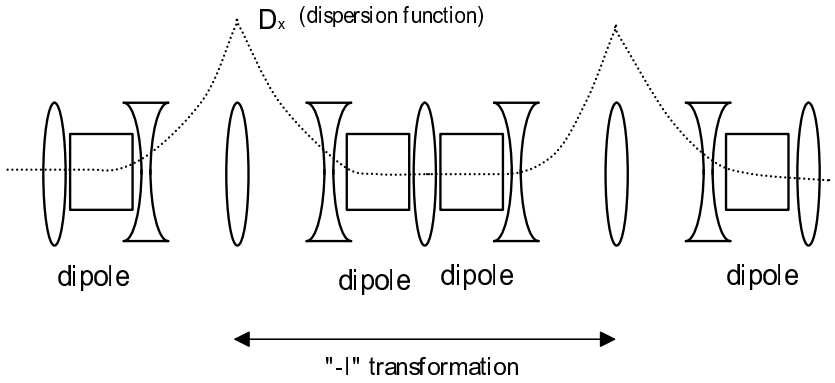

Figure 8: Schematic of collimation optics. Energy spoilers and chromatic correction sextupoles can be placed at the high-dieprsion points. The $-I$ transformation ensures that geometric aberrations from the sextupoles cancel, and also that energy errors do not convert into betatron oscillations via the collimator wake fields. Dispersion also helps for betatron collimation since it increases the beam size.

final doublet which allows collimation at a larger number of σ and thus also opens up the aperture, or (d) shorten the overall length of the collimation system.

As an illustration of a possible advantage, consider a nonlinear vertical collimation using a skew sextupole. The deflection imparted by a skew sextupole to a particle at vertical amplitude y_{sext} (assuming zero horizonal offset) is

$$\Delta y' = -\frac{K_s}{2} y_{sext}^2 \tag{19}$$

and the particle position at a downstream spoiler is $y_{spoiler} \approx R_{34}\Delta y'$, where R_{34} is the transport matrix element from the skew sextupole to the spoiler. Collimation at $n_y\sigma$ is achieved if the collimator gap is chosen as

$$g = \frac{R_{34}K_s}{2}(n_y\sigma_y)^2 = \frac{R_{34}K_s}{2} n_y^2 \beta_{y,\mathrm{sext}}\epsilon_y \ . \tag{20}$$

If the values of R_{34} and K_s are sufficiently high, the collimator gap can potentially be much larger than the linear value (18). In addition, the beta function at the spoiler does not directly enter in Eq. (20). Hence, by choosing a small beta function at the spoiler, the wake-field effects of the collimators can be made much smaller, in such a nonlinear scheme.

3 Final Focus

3.1 Purpose

The purpose of the final focus system is to demagnify the beams by a factor of 100–300 down to a few tens or hundreds of nanometers horizontally and a few nanometers vertically at the interaction point, where the beams collide.

Important design issues are the linear and nonlinear optics, the performance limitations arising from higher-order aberrations and from synchrotron radiation in dipole or quadrupole magnets, the tolerances on magnet position stability and power-converter drifts, and the luminosity tuning strategy.

3.2 Chromatic Correction

The unprecedentedly high luminosity of future linear colliders implies an extremely small beam size, which requires both small emittances and small beta functions.

The small beta functions at the collision point are realized by focusing the beam with a doublet of two strong quadrupole magnets located a few meters upstream (the doublet ensures that the beam is focused in both transverse planes, making use of the strong focusing principle). The normalized focusing strength of a quadrupole, k_q (in units of m^{-2}), depends on the particle momentum as

$$k_q = \frac{B_T}{a(B\rho)} = \frac{eB_T}{ap_0(1+\delta)} \tag{21}$$

where B_T is the pole tip field, a the pole-tip radius, $B\rho \equiv p/e$ the magnetic rigidity of the particle, p_0 the design momentum, and $\delta \equiv (p-p_0)/p_0$ the relative momentum deviation. Typical values for the final quadrupole are $B_T/a \approx 300$–500 T/m and $k_q \approx 0.1$–0.3 m^{-2}. Since the focusing strength is energy dependent, particles with slightly different energies will be focused at different distances behind the quadrupole. This is illustrated in Fig. 9.

The change in focal length with particle energy is called the chromaticity of the final focus. It can be computed as an integral over the final quadrupoles

$$\xi_y \equiv \frac{L_y^c}{\beta_y^*} = -\frac{1}{\beta_y^*}\int ds\, k_q(s) R_{34}(s)^2 \approx -\int ds \beta(s) k_q(s) \tag{22}$$

where R_{34} is the (3,4) transport matrix elements from position s to the IP which relates an an angular deflection $\Delta y'$ at s to a position shift $\Delta y^* = R_{34}\Delta y'$ at the IP. The approximate relationship is valid since the final doublet is about 90° away from the interaction point. The quantity L_y^c is called the chromatic length, and in the vertical plane, it can be limited to be only slightly larger than the free length from the exit of the final (vertically focusing) quadrupole to the IP. In the field free region around the collision point the beta function evolves as

$$\beta(s) = \beta^* + \frac{s^2}{\beta^*}\,. \tag{23}$$

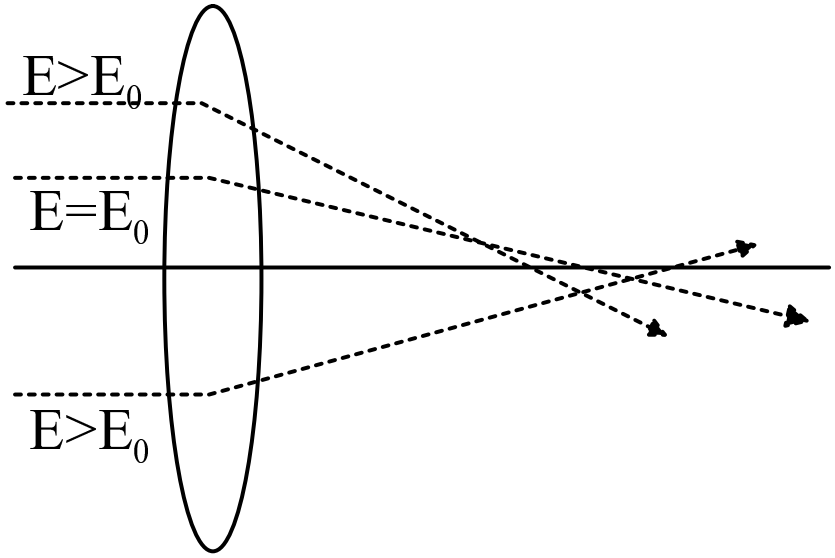

Figure 9: Schematic of a chromatic lens, where the focal length depends on the particle energy.

Since β^* is small, the IP chromaticity of a linear collider is huge, usually one or two orders of magnitude larger than the maximum chromaticities realized in storage rings..

If the chromaticity is not corrected the vertical spot size at the interaction point becomes

$$\sigma_y^* \approx \sigma_{y,0}^* \sqrt{1 + \xi_y^2 \sigma_\delta^2} \tag{24}$$

where $\sigma_{y,0}^*$ ($= \sqrt{\beta_y^* \epsilon_y}$) is the ideal linear design spot size and $\delta_{\rm rms}$ the rms energy spread. Since typically $\xi \approx 30\ 000$ and $\sigma_\delta \approx 0.28\%$, the chromaticity, if uncorrected, would increase the IP spot size by a factor of $\xi_y \sigma_\delta \approx 100$!

Therefore, chromatic correction is indispensable. As in a storage ring, this correction is performed by placing sextupoles at locations with nonzero dispersion.

The normalized strength of a sextupole in units of m^{-3} is defined as

$$k_s = \frac{1}{B\rho} \left. \frac{\partial^2}{\partial x^2} B(x) \right|_{x=0} = \frac{2B_T}{(B\rho)a^2}, \tag{25}$$

where a denotes the pole-tip radius, B_T the pole tip field at the radius a, and $B\rho$ ($= p/e$) the magnetic rigidity of the beam. The integrated sextupole strength is given by $K_s = l_s k_s$, where l_s is the length of the sextupole. Similarly, the integrated strength of the quadrupole is defined as $K_q = l_q k_q$, where l_q is the quadrupole length.

We assume for simplicity that a sextupole is placed near the final quadrupole magnet. The deflections generated by these two magnets are

$$\Delta x' \quad = \quad -\frac{K_q}{1+\delta} \left(x + D_x \delta\right) - \frac{K_s}{2(1+\delta)} \left((x + D_x \delta)^2 - y^2 \right) \tag{26}$$

$$\Delta y' \quad = \quad \frac{K_q}{1+\delta}\, y + \frac{K_s}{1+\delta}\, (x + D_x\delta) y \;, \tag{27}$$

where we have included a horizontal dispersion. In either equation, the first term describes the effect of the quadrupole and the second that of the sextupole. Expanding $1/(1+\delta) \approx (1-\delta)$ and collecting all terms linear in $x\delta$ (the coefficient of $x\delta$ corresponds to the chromaticity $\xi_{x,y}$), we find that the chromaticity is exactly zero in both planes if

$$K_s D_x = K_q \;. \tag{28}$$

However, the sextupoles introduce undesirable nonlinear terms, such as a vertical deflection which is proportional to the product xy, or a horizontal deflection proportional to x^2 and y^2.

We next estimate the importance of these nonlinear terms. The integrated quadrupole strength is roughly equal to the inverse focal length of the final doublet, *i.e.*, $K_q \approx 1/f = 1/l^*$ (here l^* is the free length between the exit of the last quadrupole and the IP).

The vertical deflection due to the nonlinear geometric term ($\propto xy$) is

$$\Delta y' \approx K_s xy \approx \frac{xy}{D_x l^*} \;. \tag{29}$$

This results in a position change at the IP of about

$$\Delta y^* \approx l^* \Delta y' \approx \frac{xy}{D_x} \;. \tag{30}$$

To obtain the corresponding increase of the IP spot size we must integrate the square of this expression over the beam distribution, and get $\Delta\sigma_y^* = \sqrt{< \Delta y^{*\,2} >}$. We also find it convenient to normalize the result to the nominal IP spot size:

$$\frac{\Delta\sigma_y^*}{\sigma_y^*} \approx \frac{\sigma_{x,q}\sigma_{y,q}}{D_x\sigma_y^*} \approx \frac{\sqrt{\beta_{x,q}\epsilon_x}\, l^*}{\beta_y^* D_x} \;, \tag{31}$$

where $\sigma_{y,q}$ and $\sigma_{x,q}$ are the rms beam sizes at the quadrupole, and $\beta_{x,q}$ is the associated horizontal beta function. The quantities with an asterisk always refer to the IP.

As an example, we insert typical NLC parameters: $\beta_{x,q} \approx 20$ km, $\epsilon_x \approx 3 \times 10^{-12}$ m, $l^* = 2$ m, $D_x \approx 0.05$ m, $\beta_y^* \approx 100$ μm, which gives

$$\frac{\Delta\sigma_y^*}{\sigma_y^*} \approx 100 \;. \tag{32}$$

Hence, the chromatic correction with single sextupoles increases the IP beam size by a factor of 100 due to the geometric aberrations that it induces! In other words, by adding a single (or two) sextupole(s) at a dispersive location we have corrected the chromatic blow up of the spot sizes, but the prize to be paid for this is a geometric blow up by also a factor of 100. Thus we need to add further sextupoles to cancel these additional aberrations. The accuracy of the cancellations must be of the order of 10^{-3}, implying tight tolerances on the optics between the sextupoles and its stability.

To cancel the large geometric aberrations, typically two pairs of sextupoles are used, for horizontal and vertical chromatic correction, respectively. The sextupole pairs are placed either near the final quadrupoles or a multiple of π in betatron-phase advance away from them. The top picture of Fig. 10 illustrates the basic layout of a classical final-focus system with modular chromatic correction section, the bottom picture the more compact advanced design.

Figure 11 shows a sextupole magnet (green and round near the center) in the chromatic correction section of the SLC final focus. The small metal roofs are part of an early SLC upgrade and protect the magnets against water dripping from the ceiling.

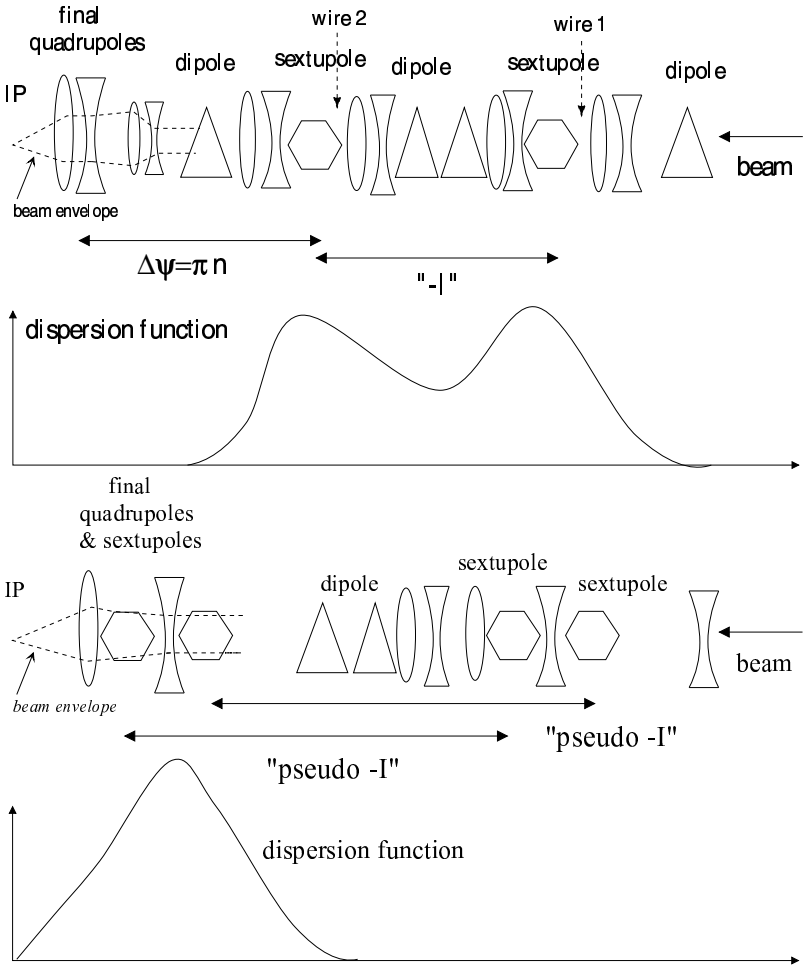

Figure 10: Schematic representation of a conventional modular (top) and advanced compact final-focus system (bottom). The beam moves from right to left. Top picture: the beam passes the chromatic correction section and then a final demagnifier, before it reaches the interaction point. Only one pair of sextupoles is shown. A similar set of sextupoles and bending magnets would be located further to the right. This scheme was invented by K. Brown. Wire scanners located near the two sextupoles, as indicated, can measure the energy-position correlation within the bunch; see homework problem 2. Bottom picture: the beam traverses two geometric sextupoles, a dipole section, and then the final doublet with an interleaved pair of chromatic-correction sextupoles, before it reaches the IP. All 4 sextupoles are shown. This compact system was invented by P. Raimondi.

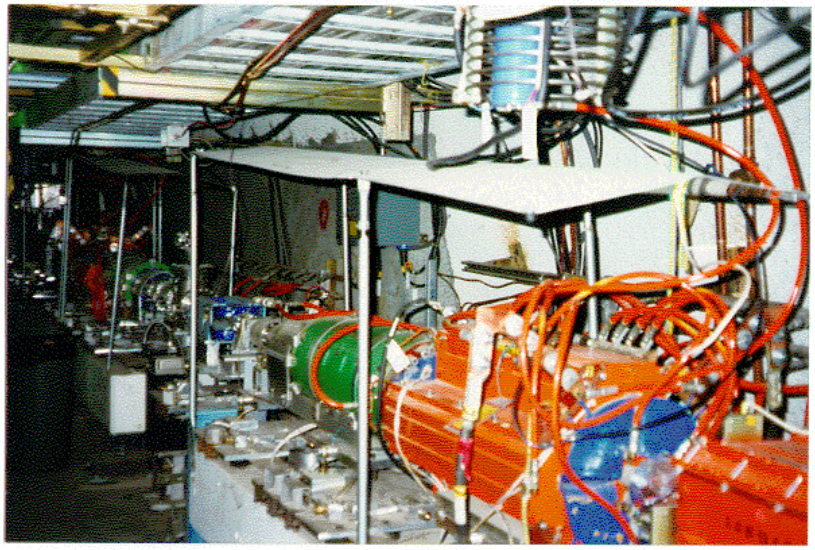

Figure 11: Photograph of the chromatic correction section in the SLC final focus.

3.3 $-I$ Transformation

An elegant way to eliminate the geometric aberrations generated by the chromatic-correction sextupoles is to place them in pairs separated by a $-I$ transformation. This scheme was invented by K. Brown. It is employed in the collimation system and in the final focus (possibly slightly modified in advanced designs, where instead of a $-I$, a 'pseudo $-I$' with $R_{12} = R_{34} = 0$ is used with similar benefits).

The linear beam transport in a single-pass system is often expressed by a (6×6) matrix relating the initial (subscript i) and final (subscript f) phase-space coordinates:

$$\begin{pmatrix} x \\ x' \\ y \\ y' \\ z \\ \delta \end{pmatrix}_f = \begin{pmatrix} R_{11} & R_{12} & R_{13} & R_{14} & R_{15} & R_{16} \\ R_{21} & R_{22} & R_{23} & R_{24} & R_{25} & R_{26} \\ R_{31} & R_{32} & R_{33} & R_{34} & R_{35} & R_{36} \\ R_{41} & R_{42} & R_{43} & R_{44} & R_{45} & R_{46} \\ R_{51} & R_{52} & R_{53} & R_{54} & R_{55} & R_{56} \\ R_{61} & R_{62} & R_{63} & R_{64} & R_{65} & R_{66} \end{pmatrix} \begin{pmatrix} x \\ x' \\ y \\ y' \\ z \\ \delta \end{pmatrix}_i . \tag{33}$$

In general we can express the position of a particle or of the beam centroid as the sum of betatron oscillation, x_β, dispersion D and higher order dispersion, $D^{(k)}$ ($k = 2, ...$), as

$$x = x_\beta + D\delta + \sum_{k \geq 2} D^{(k)} \delta^k \approx x_\beta + D\delta \, . \tag{34}$$

Often the higher-order dispersion terms ($D^{(k)}$ with $k \geq 2$) are ignored, as we will do in the following analysis.

As already mentioned, in a conventional final focus, two pairs of sextupoles are used for chromatic correction, one pair for the horizontal plane, and the other for the vertical plane. We now consider one such pair in more detail. We assume that at the location of the first sextupole the dispersion is finite, $D_i \neq 0$, but that the slope of dispersion is zero, $D_i' = 0$, and that there are no vertical bending magnets anywhere, hence $R_{36} = 0$ and $R_{46} = 0$. The (2×2) submatrices in the vertical and horizontal plane, between the two sextupoles, are commonly chosen as $-I$ (minus identity) transformations, first suggsted by K. Brown. The full R matrix between the two sextupoles forming a pair then has the form

$$\begin{pmatrix} -1 & 0 & 0 & 0 & 0 & R_{16} \\ 0 & -1 & 0 & 0 & 0 & R_{26} \\ 0 & 0 & -1 & 0 & 0 & 0 \\ 0 & 0 & 0 & -1 & 0 & 0 \\ 0 & 0 & 0 & 0 & 1 & R_{56} \\ 0 & 0 & 0 & 0 & 0 & 1 \end{pmatrix} . \tag{35}$$

We write the initial position of a particle on a dispersive trajectory as $x_i = x_{\beta,i} + D_i\delta$, and the corresponding final position as $x_f = x_{\beta,f} + D_f\delta$. From Eqs. (33) and (35) it follows that $x_{\beta,f} = -x_{\beta,i}$ and that the dispersion at the second sextupole is

$$D_f = -D_i + R_{16}. \tag{36}$$

This illustrates that without bending magnets (*i.e.*, with $R_{16} = 0$) the dispersion propagates exactly like a betatron oscillation. If there are bending magnets between the initial and final positions, in general the $(1, 6)$ matrix element is not zero, *i.e.*, $R_{16} \neq 0$, and, in particular, the strengths of the bending magnets between the sextupoles can be adjusted so that $R_{16} = 2D_i$, whence $D_f = D_i$. In addition, it is possible to design the optics such that $R_{26} = 0$, and hence $D_i' = D_f' = 0$. The last nonzero element, R_{56}, describes the change in path length for different momentum deviations. It is the analogue of the momentum compaction factor in a storage ring. Usually, R_{56} in the final focus is so small, that its effect can be ignored.

We are now in a position to formulate the idea behind the $-I$ transform. For simplicity we consider the horizontal plane only. We assume that the sextupoles are thin, so that their effect may be represented by a single nonlinear deflection, and we denote their integrated strengths by $K_{s,1}$ and $K_{s,2}$.

As before, the dispersion at the first sextupole is taken to be $D_i \neq 0$ and the slope to be zero $D_i' = 0$. We denote the particle coordinate just prior to the first sextupole by $x_i = x_\beta + D_i\delta$ (here $x_\beta \equiv x_{\beta,i}$), the associated trajectory slope by x_i', and the relative momentum deviation by δ. Behind the first sextupole the slope of the particle trajectory becomes

$$x_1' = x_i' - \frac{1}{2}K_{s,1}x_i^2 = x_0' - \frac{1}{2}K_{s,1}x_\beta^2 - K_{s,1}x_\beta D_i\delta - \frac{1}{2}K_{s,1}D_i^2\delta^2. \qquad (37)$$

In addition to the initial slope, we here recognize three nonlinear dependencies introduced by the thin sextupole. The term proportional to x_β^2 represents a geometric aberration and the component quadratic in δ a second order dispersive term. The mixed product proportional to $x_\beta\delta$ is the chromatic term, which we want to generate in order to compensate the chromaticity of the final-focus quadrupoles.

Applying the $-I$ transform, Eq. (35), with $R_{26} = 0$ and $R_{16} = 2D_i$, we obtain the particle coordinates and slopes just prior to the second sextupole:

$$x_2 = -x_\beta - D_i\delta + R_{16}\delta = -x_\beta + D_i\delta \qquad (38)$$

$$x_2' = -x_\beta' + \frac{1}{2}K_{s,1}x_i^2. \qquad (39)$$

Inserting again $x_i = x_\beta + D_i\delta$ and applying the kick from the second quadrupole, $\Delta x' = K_{s,2}x_2^2$, we obtain

$$x_2' = -x_\beta' + \frac{1}{2}K_{s,1}(x_\beta^2 + 2x_\beta D_i\delta + D_i^2\delta^2) - \frac{1}{2}K_{s,2}(x_\beta^2 - 2x_\beta D_i\delta + D_i^2\delta^2). \qquad (40)$$

For equal sextupole strengths, $K_{s,1} = K_{s,2} \equiv K_s$, the geometric aberrations and the second-order dispersion terms cancel exactly, and all that is left is the chromatic component:

$$x_2' = -x_\beta' + 2K_s x_\beta D_i\delta. \qquad (41)$$

The important conclusion is that a $-I$ pair of sextupoles, as considered here, generates only chromaticity and no other low-order aberrations. This conclusion still holds true if the vertical motion is also included in the analysis. Of course, in reality the $-I$

transform is not perfect, but itself varies with the momentum deviation. This gives rise to higher-order chromo-geometric aberrations, which ultimately limit the energy bandwidth of the final-focus system.

There is an interesting aspect of dispersion in a linear collider. In circular accelerators dispersion is normally measured by sampling off-energy orbits with beam-position monitors. In linear colliders, however, varying the energy at some point in the beam line and observing the induced change in orbit measures the R_{16} matrix element between the point of energy change and the BPMs downstream. In general this is not equal to the energy-position correlation within the bunch, as first pointed out by P. Emma. The energy-position correlation in the bunch is a result of changes in the individual particle energies,—due to acceleration, synchrotron radiation or wake fields,—and subsequent energy-dependent path lengths all along the beam line, whereas the R_{16} measurement probes the effect of a change in acceleration at one particular location only.

3.4 Performance Limitations

Usually the beam has a significant energy spread, which is introduced to provide 'BNS damping' against the effect of transverse wake fields in the linac. A typical rms energy spread is 0.3% at the entrance of the final focus, and the final-focus momentum bandwidth must be correspondingly large, of the order of 1%. A larger bandwidth would help to further stabilize the beam in the linac.

The momentum bandwidth of a final focus is commonly limited by fourth-order optical aberrations which arise because the $-I$ transformations and phase advances between elements are no longer ideal for off-energy particles, since the focusing of all quadrupoles is chromatic. In principle, the bandwidth can be increased by adding further nonlinear elements at dispersive locations, such as additional ('Brinkmann') sextupoles, octupoles, or decapoles. In practice, the alignment tolerances on these elements and operational difficulties might limit the achievable bandwidth. Most of the aberrations decrease for increasing dispersion. However, a larger dispersion implies stronger bending angles (or a longer system) and a growing importance of synchrotron radiation.

Namely, as we have indicated above, the dispersion at the chromatic-correction sextupoles is generated by bending magnets, and we are faced with the undesirable situation that we need bending magnets at the highest energy of the linear collider.

Synchrotron radiation in the dipole magnets introduces and energy spread which affects both the horizontal and vertical plane. The additional energy spread acquired in a dipole of length l_b and bending angle θ is

$$(\Delta\sigma_\delta)^2 = \frac{55}{24\sqrt{3}} r_e \lambda\!\!\!^{-}_e \gamma^5 \frac{\theta^3}{l_b^2} \ , \tag{42}$$

where $\lambda\!\!\!^{-}_e$ is the Compton wavelength of the electrons.

In the horizontal plane, the synchrotron radiation causes emittance growth similar to the effect of quantum fluctuation on the horizontal emittance in a storage ring. The additional contribution to the horizontal IP spot size and IP divergence is

$$\Delta\sigma_x^2 \quad = \quad C_q E^5 \int ds |G|^3 (R_{16}^{s\rightarrow IP})^2, \tag{43}$$

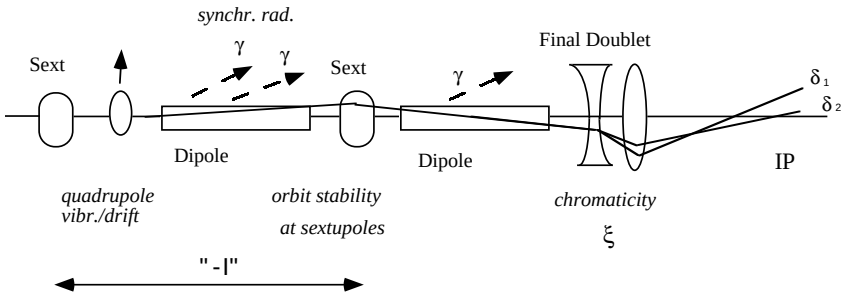

Figure 12: Schematic of a conventional final focus and its primary limitations.

$$\Delta\sigma_{x'}^2 \quad = \quad C_q E^5 \int ds |G|^3 (R_{26}^{s\rightarrow IP})^2, \tag{44}$$

$$\tag{45}$$

where $C_q = 4.13 \times 10^{-11}$ m^2 GeV^{-5}, $G = 1/\rho$ the inverse bending radius, and $R_{i6}^{s\rightarrow IP}$ the (i,6) matrix element from location s to the IP.

In either plane, the spot size is affected also by a chromatic effect, that is the synchrotron radiation introduces a change in the particle energy which (*e.g.*, after the sextupole magnets) is not chromatically corrected and which changes the particle's focal length after the final doublet. This effect can be estimated from the chromaticity $\xi_{x,y}$ of the final doublet:

$$\frac{\Delta\sigma_{x,y}}{\sigma_{x,y}} \approx \Delta\sigma_\delta \xi_{x,y} \tag{46}$$

where

$$(\Delta\sigma_\delta)^2 = C_q E^5 \int ds |G|^3 \tag{47}$$

is the energy spread induced by the last block of bending magnets. In a conventioncal final focus the upstream bending magnets tend to also contribute an additional 50% to the spot size increase. In a compact final focus the effect is reduced by a factor of $1/\sqrt{5}$, but it is not zero, since even here an energy change somewhere along the dipole is not fully chromatic corrected (but only to the extent that the dispersion at the sextupole is generated downstream of the location of photon emission).

A similar chromatic spot size increase can arise from longitudinal wake fields or space charge forces which also may change the energy distribution of the bunch between the chromatic-correction sextupoles or dipoles and the final doublet.

Figure 12 is a schematic highlighting some major limitations to the final-focus performance: synchrotron radiation and the tolerances on magnet motion.

3.5 Tolerances

Since the beams at the collision point are so small, and since we make use of strong sextupoles to cancel the chromaticity and geometric aberrations with a high precision the performance of the final focus optics is sensitive to many forms of perturbations. The calculation of tolerances is tedious, but they constitute a crucial ingredient to the viability of a collider, and in the following we present a few example calculations.

The first type of errors which are important are those related to changes in the particle trajectory, *i.e.*, due to quadrupole position jitter. A vibrating quadrupole deflects the beam so that it changes its transverse position at the collision point, and may miss the opposing beam (Fig. 13 a). Usually the tolerances are tighter in the vertical plane, due to the smaller vertical spot size. The change in IP position due to a change in a vertical quadrupole position by y_q is

$$\frac{\Delta y^*}{\sigma_y^*} = -y_q K_q \sqrt{\beta_y \epsilon_y} |\sin(\psi_y^* - \psi_{y,q})| \ , \tag{48}$$

where $K_q = k_q l_q$ is the integrated normalized quadrupole strength (l_q the length of the quadrupole), and $(\psi_y^* - \psi_{y,q})$ the betatron phase advance between the quadrupole and the IP. The tightest tolerance is almost always that for the final doublet, where an offset of y_q roughly causes an IP displacement of equal magnitude, and hence the tolerance on fast vibrations is less than a nanometer. Note also that in the final focus $|\sin(\psi_y^* - \psi_{y,q})| \approx 1$ is a good approximation for almost all locations.

All the tolerances related to the IP orbit are fast tolerances, since an IP orbit feedback can correct the IP position after a few, say 6 pulses (corresponding to about 20 Hz).

A second class of tolerances refers to the IP spot size. Corrections of the IP spot size can only be done every few minutes or so and hence these tolerances must be met over a much longer time scale. The most important aberrations increasing the IP spot size are *residual dispersion*, *waist shift* and *skew coupling*. They are illustrated in Fig. 13 b–d.

Vertical dispersion is generated by a displaced quadrupole, by rolls of bending magnets or quadrupoles, or by vertical displacements of sextupoles. For example, a quadrupole displaced by y_q will increase the IP spot size via dispersion as

$$\Delta\sigma_y^* = y_q K_q \sigma_\delta |R_{34} - T_{346}| \tag{49}$$

where two effects contribute: the chromatic dependence of the deflection and the chromatic depedence of the displaced trajectory. In Eq. (49), σ_δ is the relative rms energy spread, and T_{346} the second-order transport-matrix element which describes the second-order contribution to the shift in vertical interaction-point beam position as a function of changes in the initial slope or energy according to

$$\Delta y^* = R_{34}\Delta y' + R_{36}\Delta\delta + T_{346}\Delta\delta\Delta y' + \ldots \tag{50}$$

and in our example $\Delta y' = -K_q y_q/(1+\delta) \approx -K_q y_q(1-\delta)$. Note that $R_{34} = \sqrt{\beta_y^* \beta_{y,q}}\sin(\psi_y^* - \psi_{y,q})$, which also entered in Eq. (48).

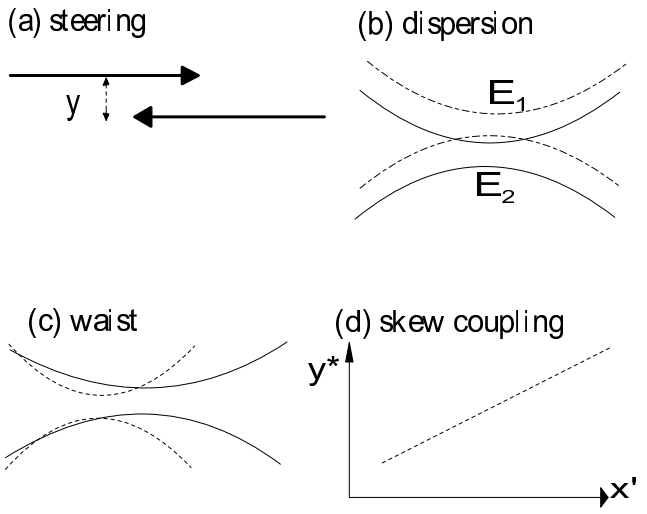

Figure 13: Steering errors and various low-order aberrations for which tolerances are calculated.

A waist shift at the collision point arises if the sextupole is horizontally displaced (or if upstream quadrupoles are displaced so as to steer the beam horizontally at the sextupole). The change in local gradient due to a horizontal offset at the sextupole x_s is $(K_s x_s)$ and this causes a change in the vertical and horizontal IP positions by

$$\Delta y^* = -K_s x_s y^{'*} R_{34}^2 \approx -K_s x_s \beta_{y,s} \beta_y^* y'^* \tag{51}$$

$$\Delta x^* = -K_s x_s x^{'*} R_{12}^2 \approx -K_s x_s \beta_{x,s} \beta_x^* x'^* \tag{52}$$

and the corresponding relative changes in the IP spot size

$$\frac{\Delta \sigma_x^*}{\sigma_{x0}^*} = K_s x_s \beta_{x,s} \tag{53}$$

$$\frac{\Delta \sigma_y^*}{\sigma_{y0}^*} = K_s x_s \beta_{y,s} \ , \tag{54}$$

where $\beta_{x,s}$ and $\beta_{y,s}$ denote the beta functions at the location of the sextupole. We can identify the associated longitudinal shift in the IP waist position as

$$\Delta w_{x,y} = -K_s x_s \beta_{x,y,s} \beta_{x,y}^* \ . \tag{55}$$

A similar waist shift is induced by a change in the strength of a quadrupole ΔK_q (simply replace $K_s x_s$ by ΔK_q to obtain the effect).

Skew coupling finally arises from rolls of the quadrupole magnets or vertical displacement of sextupoles or from trajectory errors that cause a vertical orbit offset in the

sextupoles. As an example the beam size increase due to a vertical sextupole displacement by y_s is

$$\Delta\sigma_y = y_s K_s \sigma_x |R_{34}| \tag{56}$$

where R_{34} is the matrix element from the sextupole to the IP, σ_x is the horizontal beam size at the sextupole magnet, and K_s the integrated normalized sextupole strength. Similarly a quadrupole displacement y_q which steers the beam vertical through a downstream sextupole by $\Delta y_s = R_{34}^{q\to s} y_q K_q$ will blow up the spot size by

$$\Delta\sigma_y = y_q |R_{34}^{q\to s}| K_q K_s \sigma_x |R_{34}^{s\to *}| \ . \tag{57}$$

We mention in passing that the tolerances and bandwidth limitations can be derived more elegantly using a description based on Lie algebra, which was introduced to the field of linear colliders by J. Irwin, following the pioneering work by A. Dragt. For example, the Lie generator describing a sextupole of integrated strength K_s at location s would be

$$-H = -\frac{K_s}{6}(x_s^3 - 3x_s y_s^2) \tag{58}$$

and the coordinates x_s and y_s can be transformed to the interaction point using the inverse transport matrix

$$x_s = R_{22}^{s\to *} x^* - R_{12}^{s\to *} x'^* \approx -R_{12}^{s\to *} x'^* \tag{59}$$

$$y_s = R_{44}^{s\to *} y^* - R_{34}^{s\to *} y'^* \approx -R_{34}^{s\to *} y'^* \ . \tag{60}$$

As a second example of the Lie algebra description, expressed in IP coordinates a waist shift by l corresponds to the generator

$$\frac{1}{2} l x'^{*2} \ . \tag{61}$$

Applying the Lie operator $\exp(l x'^{*2}/2)$ to x^* by utilizing Poisson brackets one indeed has

$$x^{*n} = \exp\left(\frac{1}{2} l x'^{*2}\right) x^* = x^* - l x'^* [x^*, x'^*] = x^* - l x'^* \ . \tag{62}$$

This is the equation for a waist shift by the distance l. For a thorough introduction to the Lie-algebra approach, we refer to the excellent article by J. Irwin.

3.6 Final Quadrupole

The vertical beta function at the center of the final quadrupole is about

$$\beta_q \approx \beta^* + \frac{1}{\beta^*}(l^* + l_q/2)^2 \tag{63}$$

where l_q is the length of the quadrupole. The integrated quadrupole strength is equal to the inverse focal length, which more accurately than $1/l^*$ should be written as $1/(l^* + l_q/2)$:

$$l_q k_q \approx \frac{1}{l^* + l_q/2} \ . \tag{64}$$

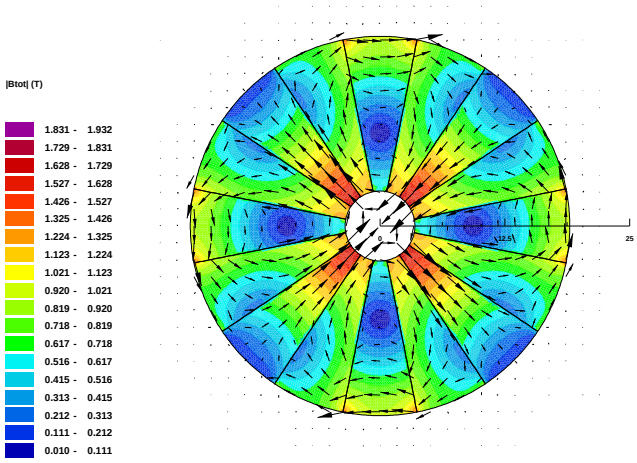

Figure 14: Cross section of a final focusing quadrupole with gradient 468 T/m for the permanent magnet material VACOMAX 225HR Sm_2Co_{17}, as computed for a 16-sector magnet by ROXIE (Courtesy: M. Aleksa, S. Russenschuck)

The chromaticity of the final quadrupole is then equal to

$$\xi \approx \beta_q k_q l_q \approx \frac{l^* + l_q/2}{\beta_y^*} \,. \tag{65}$$

Hence it is advantageous to reduce the length of the final quadrupole, which is equivalent to maximizing the gradient

$$k_q = \frac{B_T}{(B\rho)a} \tag{66}$$

where a is the pole-tip radius, B_T the pole-tip field, and $(B\rho)$ the magnetic rigidity.

An appealing solution for the final quadrupole is a design based on permanent magnets. For small apertures, these can achieve the highest possible gradients, surpassing superconducting and iron-dominated approaches. Figure 14 shows a design for the final quadrupole in CLIC which would achieve a gradient of 468 T/m with a pole-tip radius of 3.3 mm.

3.7 Oide Effect

Synchrotron radiation inside the final quadrupoles becomes important at higher beam energies.

For simplicity we first ignore the horizontal motion and the horizontal beam size. Suppose a photon of energy u is emitted at position s. The change in the IP position for the emitting particle will be

$$\Delta y^*(s) = r_{36}^p(s)\frac{u}{E} \tag{67}$$

where E is the nominal energy, and the function r_{36}^p depends on the particle trajectory. The spread in the spot for an ensemble of particles will be given by

$$\begin{aligned}(\Delta y^*)^2 &= \int ds \int du\ (\Delta y^*(s))^2 n(u,s) du \\ &= \int ds r_{36}^p(s)^2 \int du \left(\frac{u}{E}\right) n(u,s) du \end{aligned} \tag{68}$$

where $n(u,s)$ is the probability of emitting a photon with energy u. The last integral can be performed (see M. Sands) and gives

$$\int du \left(\frac{u}{E}\right)^2 n(u,s) = c_u r_E \lambda\!\!\!^{-}_e \frac{\gamma^5}{|\rho(s)|^3} \tag{69}$$

where $c_u = 55/24/\sqrt{3} \approx 1.32$ and the local bending radius is

$$\frac{1}{|\rho(s)|} = |k_q(s)||y'^* R_{34}(s)| \ . \tag{70}$$

The $r_{36}^p(s)$ function in Eq. (67) can be expressed by

$$r_{36}^p(s) = y'^* \int_0^s ds' k_q(s') R_{34}^2(s') \equiv y'^* L_y^c(s) \ . \tag{71}$$

Inserting Eqs. (70) and (71) into (68) we obtain

$$(\Delta y^*)^2 = c_u r_e \lambda\!\!\!^{-}_e \gamma^5 (y'^*)^2 \int ds (L_y^c(s))^2 |k_q(s)|^3 |y'^*|^3 |R_{34}(s)|^3 \tag{72}$$

and, by averaging over a vertical Gaussian distribution in y'^*, this becomes

$$(\Delta\sigma_y^*)^2 = \frac{16}{\sqrt{2\pi}} \sigma_{y'}^{*\,5} c_u r_e \lambda\!\!\!^{-}_e \gamma^5 \int ds (L_y^c(s))^2 |k_q(s)|^3 |R_{34}(s)|^3 \ . \tag{73}$$

We can see that the Oide effect becomes worse with increasing beam energy and with increasing divergence, setting a lower limit on the achievable beta function (or an upper limit on the acceptable divergence).

An approximate expression including the horizontal beam size was derived by J. Irwin:

$$(\Delta\sigma_y^*)^2 \approx 1.22 r_e \lambda\!\!\!^{-}_e \gamma^5 \sigma_{y'}^{*\,2} \int ds L_y^{c\,2} |k_q|^3 (7\sigma_{y'}^{*\,2} R_{34}^2 + \sigma_{x'}^{*\,2} R_{12}^2) \sqrt{\sigma_{y'}^{*\,2} R_{34}^2 + \sigma_{x'}^{*\,2} R_{12}^2} \ . \tag{74}$$

The additional contribution from σ_x can be made relatively small by decreasing the strength of the horizontally focusing quadrupole. For a 3-TeV CLIC the spot-size increase due to the Oide effect is about 30%.

The probability of radiating photons is comparable to 1 and, hence, the changes in the rms spot size calculated above tend to overestimate the actual loss in luminosity.

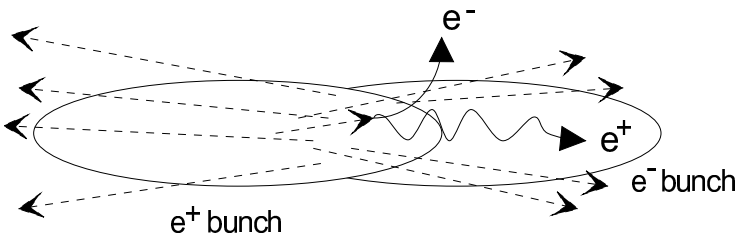

Figure 15: During the bunch collision, e^+ and e^- are strongly bent and emit beamstrahlung photons, which can convert into pairs.

4 Collisions and Luminosity

4.1 Luminosity

Assuming Gaussian bunch distributions and ignoring the variation of beam sizes during collision, *e.g.*, due to the hourglass effect (depth of focus) or due to beam-beam forces (pinch enhancement), the luminosity of a linear collider can be written as

$$L = \frac{f_{\rm rep} n_b N_b^2}{4\pi\sigma_x^*\sigma_y^*} \tag{75}$$

where $f_{\rm rep}$ denotes the repetition rate at which beam and rf are sent through the linac, n_b the number of bunches per rf pulse, N_b the number of particles per bunch, σ_x^* the rms horizontal beam size, and σ_y^* the rms vertical beam size at the interaction point.

4.2 Beam-Beam Effects

During collision, individual electrons or positrons emit synchrotron radiation in the strong field of the opposing beam, as is illustrated in Fig. 15.

This radiation is called beamstrahlung. To preserve an adequate energy spectrum of the luminosity, the number of beamstrahlung photons emitted per electron, N_γ, must be limited to a value of the order of one. Considering this constraint and assuming flat beams with $\sigma_x^* \gg \sigma_y^*$, following a recipe by R. Brinkmann we can re-express the above luminosity formula as

$$L \approx \left(\frac{5}{r_e}\right) \frac{P_{\rm wall}}{E_{\rm b}} N_\gamma \, \frac{\eta}{\sigma_y^*} \tag{76}$$

where r_e is the classical electron radius, $P_{\rm wall}$ the wall-plug power, $E_{\rm b}$ the final beam energy, and η the conversion efficiency of wall-plug power into average beam power ($P_{\rm beam} = f_{\rm rep} E_{\rm b} N_b n_b$). The beam energy is fixed by the physics requirements, and the wall plug power is limited by economic reasons. Hence, there are only two free parameters that can be optimized for maximum luminosity: the conversion efficiency η and the vertical spot size σ_y^*.

At the SLC the parameter η was much smaller than 1%. For all future projects it is raised to roughly 10%, for example, by increasing the number of bunches per rf pulse from 1 to about 100, and by improving the efficiency of all rf components.

The vertical spot size is the second free parameter. In all proposed designs, it is more than 100 times smaller than at the SLC. Such tiny spot sizes are achieved both by much reduced emittances and by interaction-point beta functions that are squeezed down to about 100 μm, as shown in Table 1.

Let us take a closer look at beamstrahlung. The typical energy of the beamstrahlung photons is characterized by the parameter Υ. This is equal to two thirds of the classical critical energy divided by the beam energy $E_{\rm b}$,

$$\Upsilon = \frac{2}{3}\frac{\hbar\omega_c}{E_{\rm b}} \approx \frac{5}{6}\frac{\gamma r_e^2 N}{\alpha\sigma_z(\sigma_x+\sigma_y)}, \tag{77}$$

where α denotes the fine structure constant. For synchrotron radiation emitted from a dipole magnet the critical freqency is $\omega_c = \frac{3}{2}c\gamma^3/\rho$ and, usually, the energy of synchrotron radiation photons is much smaller than the beam energy $\hbar\omega_c \ll E_{\rm b}$. For the beamstrahlung emitted during the beam-beam collision, this need not be the case. Typical values of Υ at the interaction point are 2×10^{-3} for the SLC, 0.3 for the NLC, and almost 10 for CLIC. If Υ becomes comparable to 1 or larger, a significant portion of beamstrahlung photons convert into real electron-positron pairs in the strong electromagnetic fields of the two beams. Unfortunately, linear colliders at multi-TeV energies can hardly avoid operating in this regime.

Besides Υ, there is a second parameter of interest, namely the number of beamstrahlung photons emitted per electron. It is

$$N_\gamma \approx \frac{5}{2}\frac{\alpha\sigma_z}{\gamma\lambda\!\!\!^{-}_e}\Upsilon\left[\frac{1}{(1+\Upsilon^{2/3})^{1/2}}\right] \approx 2\frac{\alpha r_e N_b}{\sigma_x+\sigma_y}. \tag{78}$$

The last approximation applies if Υ is small. For example, choosing $N = 10^{10}$ and $N_\gamma = 1$, we obtain $(\sigma_x+\sigma_y) \approx 400$ nm, consistent with the NLC parameter set.

Note that by reducing the bunch length σ_z, we can reach a parameter regime where Υ is large and the spot size small, but where we can still ensure that $N_\gamma \leq 1$, thanks to the quantum correction term — the brackets — of Eq. (78). This is sometimes referred to as the quantum suppression of beamstrahlung. It arises, roughly speaking, from the fact that the electrons cannot radiate photons of energy higher than the beam energy. The classical spectrum of synchrotron-radiation photon energies is modified in this extreme quantum regime.

Two further quantities characterizing beamstrahlung are the average energy loss per electron,

$$\delta_B \approx \frac{1}{2}N_\gamma\Upsilon\left[\frac{(1+\Upsilon^{2/3})^{1/2}}{(1+(1.5\Upsilon)^{2/3})^2}\right], \tag{79}$$

and the fraction of luminosity at the nominal energy,

$$\frac{\Delta L}{L} \approx \frac{1}{N_\gamma^2}\left(1-e^{-N_\gamma}\right)^2, \tag{80}$$

which depends only on N_γ. The value of $\Delta L/L$ drops rapidly for increasing N_γ, *e.g.*, for $N_\gamma = 1$, it is 81%, for $N_\gamma = 2$ only 25%, and for $N_\gamma = 3$ barely 11%.

Introducing the aspect ratio $r \equiv \sigma_y/\sigma_x$, the number of beamstrahlung photons scales as $N_\gamma \propto N_b/(\sigma_x(1+r))$ and the luminosity as $L \propto N_b N_\gamma (1+r)/r$. Hence, in order to maximize the luminosity while at the same time constraining the number of beamstrahlung photons, it is best to operate with flat beams where $r \ll 1$.

Flat-beam parameters have been adopted for all future linear collider designs. Various other and more exotic methods of overcoming the beamstrahlung problem have been proposed, such as 4-beam collisions (2 electron beams colliding with 2 positron beams, so that the net electric and magnetic fields are zero), plasma (where the plasma return current cancels the beam fields), and photon-photon collisions (here the beam energy is converted into photon energy by Compton scattering off a high-power laser). None of these advanced schemes has yet been demonstrated experimentally.

4.3 Crossing Angle

A crossing angle is used by NLC, JLC and CLIC to separate the incoming and outgoing beams and to provide a passage for the disrupted spent beam so that it can escape from the interaction region. If the crossing angle is sufficiently large, the spent beam passes outside of the final quadrupole for the incoming beam.

A large crossing angle is also needed to avoid the so-called multi-bunch kink instability, whereby an initial vertical offset between two bunches is amplified via the parasitic encounters on either side of the main collision point. If the two bunch trains enter with a relative offset δ, the offset of the two first colliding bunches is equal to δ, so that

$$y^*_{1,+} - y^*_{1,-} = \delta \ . \tag{81}$$

This will deflect the first e^- bunch vertically by

$$\Delta y'^*_{1,-} = \frac{1}{2}\frac{D_y}{\sigma_z}\delta \tag{82}$$

and the first e^+ bunch by

$$\Delta y'^*_{1,+} = -\frac{1}{2}\frac{D_y}{\sigma_z}\delta \ , \tag{83}$$

where

$$D_{x,y} = \frac{2N_b r_e \sigma_z}{\gamma \sigma^*_{x,y}(\sigma^*_x + \sigma^*_y)} \tag{84}$$

denotes the disruption parameter. The second e^- bunch will undergo a parasitic (long-range) collision with the first e^+ bunch at a distance L from the primary IP. The horizontal separation of the two bunches here is $d = L\theta_c$ and the e^+ bunch is vertically offset by $\Delta y'^*_{1,+} L$. The second e^- bunch thus experiences a vertical deflection of

$$\Delta y'_{2,-} \approx \frac{2Nr_e}{\gamma d^2} L \Delta y'^*_{1,+} \ . \tag{85}$$

Similarly, we find for the second e^+ bunch

$$\Delta y'_{2,+} \approx \frac{2Nr_e}{\gamma d^2} L \Delta y'^*_{1,-} \, . \tag{86}$$

which increases the offset at the main IP to

$$y^*_{2,+} - y^*_{2,-} = \delta + (\Delta y'_{2,+} - \Delta y'_{2,-})L = \delta + D_x D_y \left(\frac{\sigma_x^2}{\theta_c^2 \sigma_z^2} \right) \delta \, . \tag{87}$$

More generally, for the nth pair of bunches, the offset increases as

$$y^*_{2,+} - y^*_{2,-} = (1 + C)^{n-1} \delta \tag{88}$$

where

$$C = D_x D_y \left(\frac{\sigma_x^2}{\theta_c^2 \sigma_z^2} \right) \, . \tag{89}$$

We conclude that the kink multi-bunch instability is weak as long as

$$(n_b - 1)C = (n_b - 1) \frac{\sigma_x^2 D_x D_y}{\theta_c^2 \sigma_z^2} \ll 1 \, , \tag{90}$$

where in this case n_b denotes the number of bunches that interact in the free space around the interaction point, *i.e.*,

$$n_b = 1 + \frac{2l^*}{\Delta_b} \tag{91}$$

with Δ_b designating the bunch spacing and l^* the free distance between the end of the last quadrupole and the interaction point.

Chen and Yokoya, who also take into account the beam-beam effects during the head-on collision, developed a slightly modified condition for avoiding a significant vertical displacement due to the multibunch kink instability, namely

$$(n_b - 1) \ll \frac{\theta_c^2 \sigma_z^2}{\sigma_x^2 D_x D_y} \sqrt{\frac{1}{2} + \frac{D_y}{3}} \, . \tag{92}$$

Finally, the interaction point is normally located inside the strong magnetic solenoid field of the detector. If the beam passes through this solenoid under a horizontal angle, it is deflected vertically. This generates vertical dispersion and also initiates the emission of synchrotron radiation. The vertical spot size increase due to synchrotron radiation in the body of the solenoid was computed by J. Irwin similar to the Oide effect, with the result

$$\frac{\Delta {\sigma_y^*}^2}{\sigma_y^*} = \frac{c_u r_e \lambda\!\!\!^{-}_e \gamma^5}{{\sigma_y^*}^2} \int ds R_{36}(s)^2 \left| \frac{1}{\rho(s)} \right|^3 = \frac{1}{20} \frac{c_u r_e \lambda\!\!\!^{-}_e}{{\sigma_y^*}^2} \left(\frac{B_s \theta_c l^* \gamma}{2B\rho} \right)^5 \, . \tag{93}$$

A larger effect can arise from the fringe field of the solenoid. This is illustrated in Fig. 16, a simulation example for CLIC, which shows the dependence of the vertical blow up on the crossing angle, the solenoid field and the longitudinal extent of the fringe.

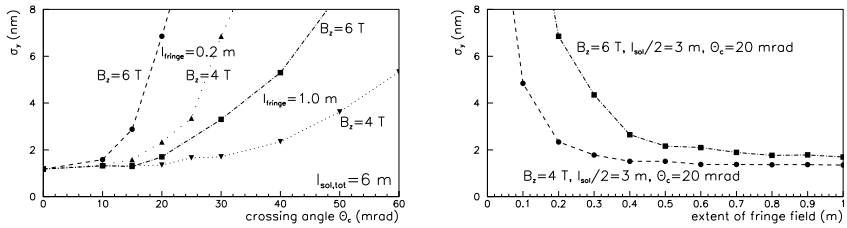

Figure 16: Simulated vertical spot size σ_y^* at the CLIC collision point vs. θ_c (left) and vs. length of fringe field (right), considering solenoid fields of 4 and 6 T.

4.4 Crab Cavity

If the bunches are collided with a horizontal crossing angle a large part of the luminisity can be lost. This loss can roughly be estimated as

$$\frac{L}{L_0} \approx \frac{1}{\sqrt{1+(\frac{\theta_c \sigma_z}{2\sigma_x})^2}} \tag{94}$$

where L_0 is the ideal luminosity for head-on collision and L the luminosity with full crossing angle θ_c. If $\theta_c \sigma_z/(2\sigma_x) \geq 1$, it is quite substantial. For CLIC this factor is about 8; hence witthout further action, the luminosity would be almost 10 times smaller than for head-on collisions of the same beams.

One way to recover the luminosity is to employ crab cavities, first suggested by R. Palmer. These deflect the head and tail of the bunch in opposite horizontal direction such that after a distance L equal to that between the crab cavity and the collision point, the two bunches are perfectly aligned with respect to each other (see Fig. 17).

The effect of the crabbing should be

$$\frac{\partial x^*}{\partial z} = \frac{\theta_c}{2} \,. \tag{95}$$

Considering an rf wave $V_{\rm rf} = V_{\rm max} \sin k_{\rm rf} z$ (bunch center passes at the zero crossing), the cavity deflects by an angle

$$\Delta x' \approx \frac{eV_{\rm max} k_{\rm rf}}{E} z \,. \tag{96}$$

The kick is transformed into an offset at the collision point via

$$\Delta x^* = R_{12} \Delta x' \,, \tag{97}$$

where R_{12} is the optical (1,2) transport matrix element. Equation (95) then yields

$$\frac{\theta_c}{2} = R_{12} \frac{eV_{\rm max} k_{\rm rf}}{E} \tag{98}$$

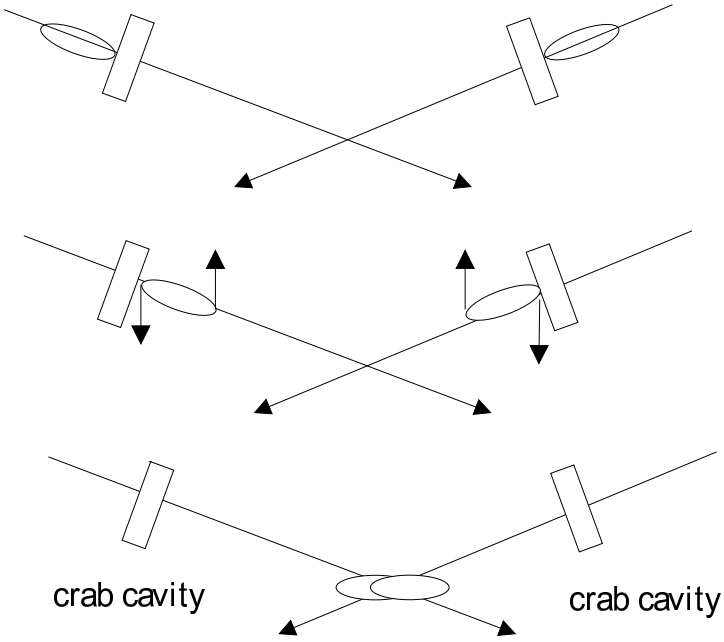

Figure 17: Schematic of crab crossing, employing dipole-mode rf cavities to rotate the beam at the collision point.

For example, with $R \approx 25$ m and $\theta_c = 20$ mrad, a voltage of 1 MV would be required at 30 GHz.

There is a tight tolerance on the relative phase stability of the two crab cavities on either side of the IP. If this phase jitters, the collision will no longer be head on. The tolerance for a 2% luminosity loss is

$$\Delta z < \frac{4\sigma_x}{5\theta_c} \tag{99}$$

or

$$\Delta\phi_{\rm rf} < k_{\rm rf}\frac{4\sigma_x}{5\theta_c}\ . \tag{100}$$

This amounts to less than 0.1° and would be tighter still at lower rf frequencies.

For fun, we can compare this with the only other project contemplating the use of crab cavities, for which actual prototypes have already been built, namely the KEK B factory. Here, the (s.c.) crab cavity frequency is 500 MHz, the crossing angle $\theta_c = 11$ mrad, and $\sigma_x = 200$ μm. The tolerance is $\Delta\phi_{\rm rf} < 8^\circ$, much looser than in a linear collider (although in a ring collider multi-turn effects might accrue).

4.5 IP Orbit Feedback

The beams can be held in collision by a fast feedback utilizing the beam-beam deflection angle as a measure of the beam-beam offset. The deflection angle is inferred by measuring the orbit at two (or more) BPMs in front of the IP and two (or more) BPMs after the IP. Each set of two BPMs defines a line, for the incoming and outgoing beam, respectively. The difference in slope between these two lines equals the deflection angle. Electronic or mechanical offsets in the BPM readouts can be eliminated by taking data for non-colliding beams (zero deflection) as a reference.

A typical beam-beam deflection scan from the SLC is shown in Fig. 18. Near the origin the centroid deflection depends almost linearly on the centroid-to-centroid offset as

$$< \Delta y' >= \frac{2N_b r_e}{\gamma\Sigma_y^*(\Sigma_x^* + \Sigma_y^*)} < \Delta y > \tag{101}$$

where $\Sigma_{x,y} \equiv \sqrt{{\sigma^{e^+}_{x,y}}^2 + {\sigma^{e^-}_{x,y}}^2}$ is the convoluted beam size. This is almost the same formula as for the deflection of a single particle, except that the single-beam spot sizes are replaced by the 'cap sigmas' (the convoluted spot sizes). The slope of the deflection scan near the origin measures the convoluted beam size, and has been used for estimating the luminosity as well as for tuning.

From a fit of the full nonlinear deflection curve to a theoretical expression, both the horizontal and vertical convoluted spot sizes can be inferred. Redundant information comes from a deflection scan in the horizontal plane. However, these signals do not provide any informations about which of the two beams is larger and thus should be corrected. For this reason, at the SLC a laser wire scanner was installed near the IP, which could measure the single-beam spot size. Also the beamstrahlung induced energy loss was found to be sensitive to the single-beam sizes, *e.g.*, a larger beam passing

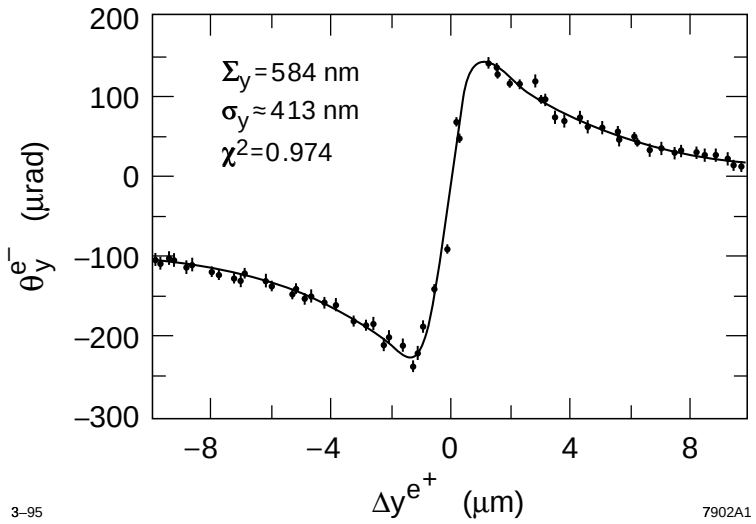

Figure 18: Vertical beam-beam deflection scan at low current, demonstrating a single-beam size of about 410 nm.

through the field of a smaller beam loses more energy, which can be detected by BPMs at dispersive locations or by dedicated photon monitors.

From the measured deflection angle, the separation of the two beams can be computed and then corrected on subsequent beam pulses using fast steering magnets. This is known under the name IP collision feedback. Figure 19 shows the simulated response of the SLC collision feedback to a small step change in the beam-beam offset. Note that the error is almost perfectly corrected after about 40 ms, or 6 pulses.

It is interesting that the collision point feedback even converges if the initial offset of the two beams is much larger than the rms beam size, *i.e.*, where the deflection scan has a slope opposite to that in the central region. Because the feedback does not know that the offset is on the other side of the extremum, the correction steps are too small in this case, and it takes a lot longer before the beams are brought back to the head-on collision. However, the algorithm is stable and always converges to the correct solution in the end.

4.6 Spot Size Tuning

We have seen that magnet motion in the final focus system can introduce waist shifts, dispersion, or skew coupling at the collision point. All of these will increase the IP spot size. It is therefore necessary to correct and cancel these aberrations on a time scale comparable to the degradation time. This concept is illustrated in Fig. 20.

The optimization can be done by scanning orthogonal tuning knobs, which *e.g.* either change the horizontal waist position or the vertical dispersion of one beam etc. The orthogonality helps to increase the speed of convergence. For example, an orthogonal

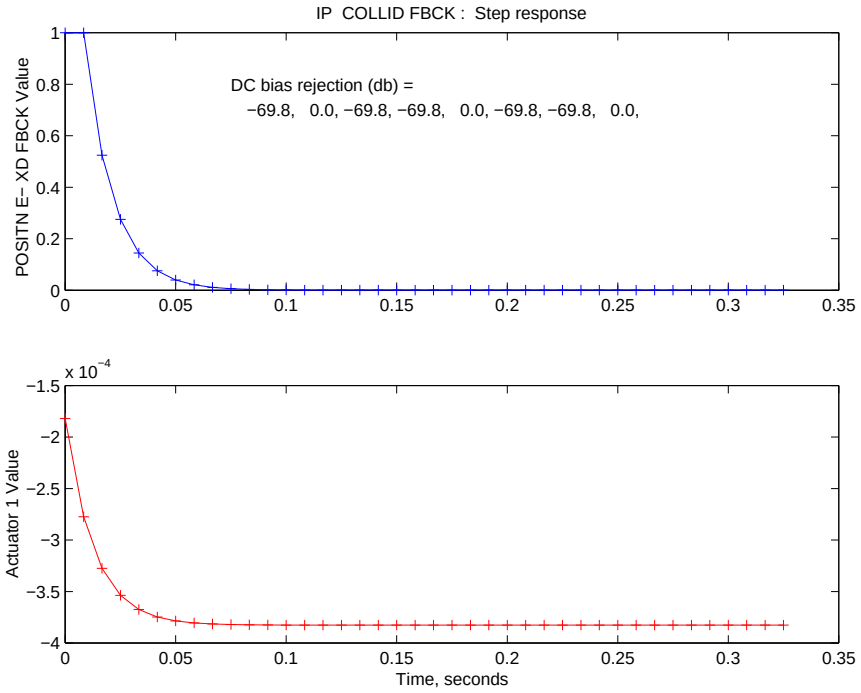

Figure 19: Simulated time response to a step change of the post-1996 SLC IP collision feedback (Courtesy L. Hendrickson). Top plot shows the feedback value - the measured offset; the bottom plot shows the change in the corrector ('actuator') strength used to steer the beams back into collision.

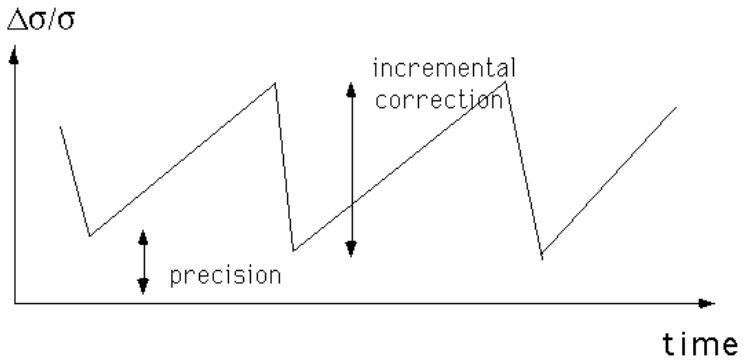

Figure 20: Schematic of tuning effect and spot-size increase between tunings.

horizontal waist knob of strength l_x would have the properties

$$\begin{aligned} \Delta x^* &= -l_x x'^* && (102)\\ \Delta x'^* &= 0 && (103)\\ \Delta y^* &= 0 && (104)\\ \Delta y'^* &= 0\,, && (105) \end{aligned}$$

and an orthogonal vertical dispersion knob of strength D_y^*

$$\begin{aligned} \Delta x^* &= 0 && (106)\\ \Delta x'^* &= 0 && (107)\\ \Delta y^* &= D_y^*\delta && (108)\\ \Delta y'^* &= 0\,. && (109) \end{aligned}$$

How does one construct a tuning knob? The problem can be cast into a matrix equation of the form:

$$\left(\begin{array}{c} \Delta\beta_x \\ \Delta\alpha_x \\ \Delta\mu_x \\ \Delta D_x \\ \Delta D'_x \\ \Delta\beta_y \\ \Delta\alpha_y \\ \Delta\mu_y \\ \Delta D_y \\ \Delta D'_y \\ \cdots \end{array}\right)_{s=s_0} = \left(\begin{array}{cccc} B_{11} & B_{12} & \ldots & B_{1N} \\ B_{21} & B_{22} & \ldots & B_{2N} \\ & \cdots & \cdots & \\ B_{M1} & B_{M2} & \ldots & B_{MN} \end{array}\right) \left(\begin{array}{c} \Delta K_1 \\ \Delta K_2 \\ \cdots \\ \Delta K_N \end{array}\right)\,. \qquad (110)$$

The sensitivity matrix $\mathbf{B}$ could either be obtained from an optics model, or it could be determined empirically on the machine. For a good solution, the number of adjustable parameters (quadrupole strengths ΔK_i) should be larger or equal to the number of constraints. So, unless one can exploit some optical symmetry one must have $N \geq M$. The matrix equation can be solved for example using a singular-value decomposition, which is a powerful tool and simultaneously minimizes the overall magnitude of the changes, *i.e.*, the sum $\sum \Delta K_i^2$.

The singular value decomposition (SVD) represents the matrix $\mathbf{B}$ as

$$\mathbf{B} = \mathbf{U} \cdot \left(\begin{array}{cccc} w_1 & 0 & \ldots & 0 \\ 0 & w_2 & \ldots & 0 \\ & \cdots & \cdots & \\ 0 & 0 & \ldots & w_N \end{array}\right) \cdot \mathbf{V}^t \qquad (111)$$

The column vectors of the $M \times N$ matrix $\mathbf{U}$ and the $N \times N$ matrix $\mathbf{V}$ are orthonormal:

$$\begin{aligned} \mathbf{U}^t \cdot \mathbf{U} &= \mathbf{I}_N && (112)\\ \mathbf{V}^t \cdot \mathbf{V} &= \mathbf{I}_N && (113) \end{aligned}$$

where $\mathbf{I}_N$ denotes the unity $N \times N$ matrix. The formal solution to Eq. (110) is

$$\mathbf{\Delta K} = \mathbf{B}^{-1}\mathbf{\Delta}\beta = \mathbf{V} \cdot \begin{pmatrix} 1/w_1 & 0 & \dots & 0 \\ 0 & 1/w_2 & \dots & 0 \\ & \dots & \dots & \\ 0 & 0 & \dots & 1/w_N \end{pmatrix} \cdot \mathbf{U}^t \ , \qquad (114)$$

where we have introduced the symbol $\mathbf{\Delta}\beta$ to denote the vector with the desired optical changes on the left side of Eq. (110). If one of the w_i is zero or small (indicating a degeneracy), its inverse must be set to zero in Eq. (114).

In order to optimize the aberrations one needs not only a knob but also a signal. For a long time, at the SLC, the aberrations were optimized by minimizing the beam size inferred from deflection scans as a function of the knob setting.

For instance, the beam size was measured for different values of the horizontal waist. The square of the measured beam size was plotted versus the waist knob setting, and the resulting curve fitted to a parabola. The knob was then set to the minimum of the parabola and subsequently the next knob optimized. In total five knobs per beam were routinely scanned and optimized every few hours by the SLC operators. However, it turned out that the resolution of the deflection scans was poor and the typically applied waist corrections, comparable to $\beta^*_{x,y}$, were mainly due to the large measurement error.

The deflection scans were finally replaced by an automatic dither feedback which made fast up-down step changes to the knob settings and correlated these changes with the response of fast luminosity signals (either beamstrahlung or radiated Bhabha events). An example is shown in Fig. 22. The new method, proposed and implemented by P. Raimondi and L. Hendrickson, was faster, more accurate, and less invasive than the previous technique based on deflections. In addition it was fully automatic. The change in the luminosity tuning procedure and its automation was one of the key factors which pushed up the SLC luminosity in its last two years of operation.

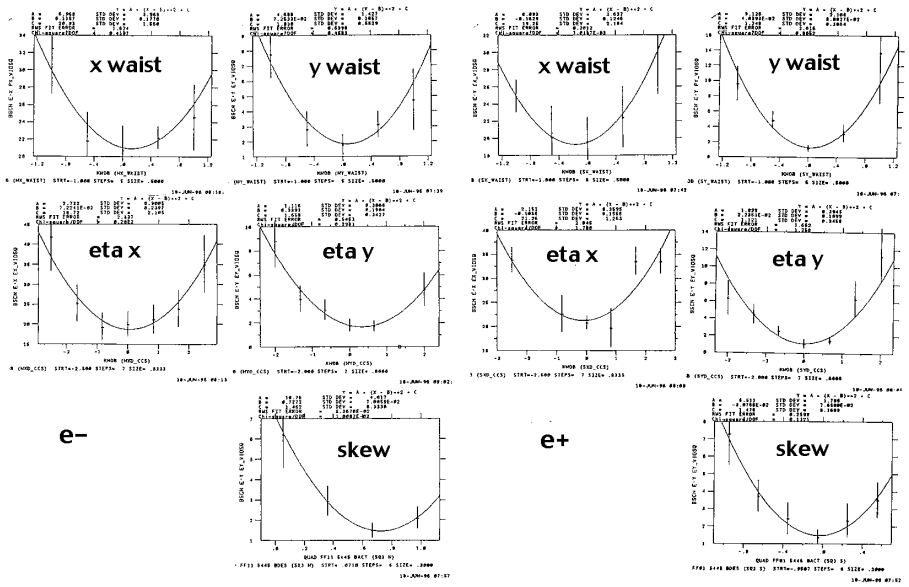

Figure 21: Aberration scans at the SLC collision point. In total, 10 aberrations had to be controlled: horizontal and vertical dispersion and waist position, as well as coupling from the horizontal into the vertical plane, for either beam. These aberrations were corrected using different combinations of quadrupole and skew quadrupole magnets, which form orthogonal multiknobs. Each multiknob was adjusted so as to optimize the IP spot size, based on a parabolic fit to the beam sizes (squared) measured for different knob values. Until 1997, the beam size was inferred from the beam-beam deflection scans, with results as shown in the figure. The errors were significant. In the last two years, the aberrations were controlled by an automatic 'dither' feedback, which made up/down changes to the multiknobs, and determined their effect on the luminosity from the correlated variation of the beamstrahlung-induced energy loss or other luminosity-related signals, such as radiative Bhabha events.

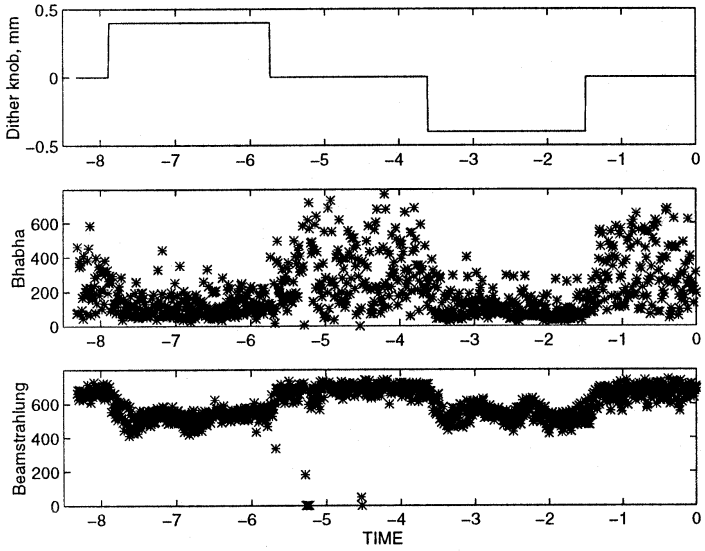

Figure 22: SLC luminosity optimization feedback: responses of radiated Bhabha luminosity monitor and beamstrahlung detector to actuator dithering (L. Hendrickson, P. Raimondi, 1997).

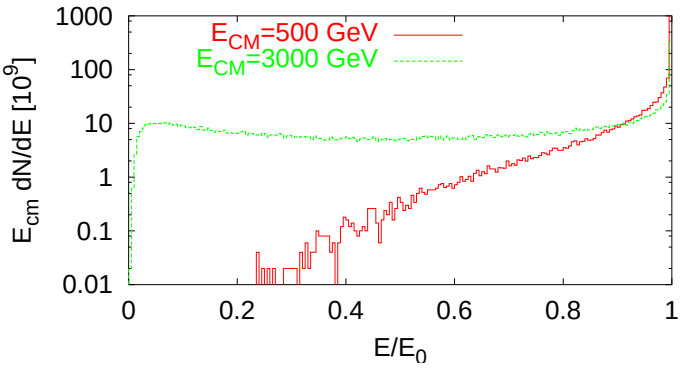

Figure 23: Energy distribution of the spent beam for centre-of-mass energies 3 TeV and 500 GeV, simulated by D. Schulte using the code Guinea-Pig.

5 Spent Beam

After the collision the beam acquires a large angular spread. In the case of CLIC the particles emerging at largest angles are oppositely charged (coherent) pairs, requiring a free-space exit cone of at least ± 10 mrad around the center line.

A second problem with the spent beam is its huge energy spread. This energy spread increases rapidly for higher beam energies, as illustrated in Fig. 23. It seems unlikely that a focusing optics can be found for a beam with nearly 100% energy spread. Hence, for the CLIC exit beam line we presently foresee only a simple chicane, which separates the charges and allows for diagnostics of the spent-beam energy spread. After the chicane the charged particle debris and the beamstrahlung photons are disposed onto a common beam dump. This is illustrated in Fig. 24.

In order that the dump is not destroyed by the beam impact and also that the latter does not generate significant acoustic waves, a dump based on water at a nominal temperature 4°C (zero thermal expansion coefficient) was proposed for CLIC by J.B. Jeanneret.

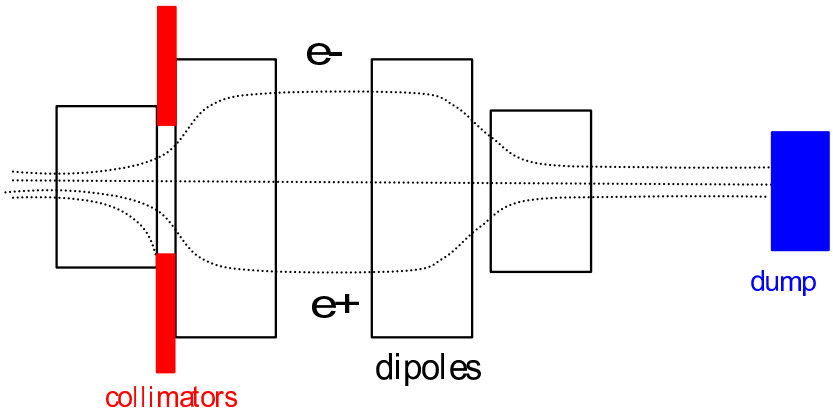

Figure 24: Schematic layout of a CLIC exit line which separates charged and neutral debris components using a chicane prior to disposal on a beam dump.